



# Understanding Interlayer Coupling in TMD-hBN Heterostructure by Raman Spectroscopy

Li Ding, Muhammad Shoufie Ukhtary, Mikhail Chubarov, Tanushree H. Choudhury, Fu Zhang, Rui Yang, *Member, IEEE*, Ao Zhang, Jonathan A. Fan<sup>1b</sup>, Mauricio Terrones, Joan M. Redwing, Teng Yang, Mingda Li, Riichiro Saito, and Shengxi Huang

**Abstract**—In 2D van der Waals heterostructures, interactions between atomic layers dramatically change the vibrational properties of the hybrid system and demonstrate several interesting phenomena that are absent in individual materials. In this paper, we have investigated the vibrational

properties of the heterostructure between transition metal dichalcogenide (TMD) and hexagonal boron nitride (hBN) on gold film at low- and high-frequency ranges by Raman spectroscopy. Nineteen Raman modes have been observed from the sample, including a new interlayer coupling mode at  $28.8 \text{ cm}^{-1}$ . Compared to reported experimental results of tungsten disulfide ( $\text{WS}_2$ ) on  $\text{SiO}_2/\text{Si}$  substrates, the Raman spectrum for  $\text{WS}_2$  on hBN/Au emerges a blue shift of about  $8 \text{ cm}^{-1}$ . Furthermore, a remarkable enhancement of Raman intensity can be obtained when tuning hBN thickness in the heterostructure. Through systematic first-principles calculations, numerical simulations, and analytical calculations, we find that the  $28.8 \text{ cm}^{-1}$  mode originates from the shearing motion between monolayer TMD and hBN layers. In addition, the gold substrate and hBN layers form an optical cavity and the cavity interference effects enhance the obtained Raman intensity. This paper demonstrates the novel vibrational modes of 2D van der Waals heterostructure as an effective tool to characterize a variety of such heterostructures and reveals a new method to enhance the Raman response of 2D materials.

Manuscript received May 3, 2018; revised June 3, 2018; accepted June 9, 2018. The work of L. Ding and S. Huang was supported by the Electrical Engineering Department and the Materials Research Institute, The Pennsylvania State University. The work of M. S. Ukhtary and R. Saito was supported by JSPS KAKENHI under Grants JP18J10199 and JP18H01810. The work of M. Chubarov, T. H. Choudhury, and J. M. Redwing was supported by The Pennsylvania State University 2D Crystal Consortium—Materials Innovation Platform (2DCC-MIP) under NSF Cooperative Agreement DMR-1539916. The work of F. Zhang and M. Terrones was supported by the National Science Foundation through the IUCRC Center for Atomically Thin Multifunctional Coatings (ATOMIC) under Grant IIP-1540018. The work of R. Yang and J. A. Fan was supported by the Air Force Office of Scientific Research Multidisciplinary University Research Initiative (MURI) under Award FA9550-16-1-0031. The work of T. Yang was supported in part by the National Key Program of China under Grant 2017YFA0206301 and in part by the Major Program of Aerospace Advanced Manufacturing Technology Research Foundation NSFC and CASC, China, under Grant U1537204. The review of this paper was arranged by Editor S. Das. (Corresponding author: Shengxi Huang.)

L. Ding and S. Huang are with the Electrical Engineering Department, The Pennsylvania State University, University Park, PA 16802 USA (e-mail: sjh5899@psu.edu).

M. S. Ukhtary and R. Saito are with the Department of Physics, Tohoku University, Sendai 980-8578, Japan.

M. Chubarov and T. H. Choudhury are with the 2D Crystal Consortium—Materials Innovation Platform, Materials Research Institute, The Pennsylvania State University, University Park, PA 16802 USA.

F. Zhang is with the Department of Materials Science and Engineering, The Pennsylvania State University, University Park, PA 16802 USA.

R. Yang and J. A. Fan are with the Department of Electrical Engineering, Stanford University, Stanford, CA 94305 USA.

A. Zhang is with the School of Materials Science and Engineering, Tsinghua University, Beijing 100084, China.

M. Terrones is with the Department of Physics, The Pennsylvania State University, University Park, PA 16802 USA, also with the Department of Chemistry, The Pennsylvania State University, University Park, PA 16802 USA, and also with the Department of Materials Science and Engineering, Pennsylvania State University, University Park, PA 16802 USA.

J. M. Redwing is with Department of Materials Science and Engineering, The Pennsylvania State University, University Park, PA 16802 USA and also with the 2D Crystal Consortium—Materials Innovation Platform, Materials Research Institute, The Pennsylvania State University, University Park, PA 16802 USA.

T. Yang is with the Shenyang National Laboratory for Materials Science, Institute of Metal Research, Chinese Academy of Sciences, Shenyang 110016, China.

M. Li is with the Department of Nuclear Science and Engineering, Massachusetts Institute of Technology, Cambridge, MA 02139 USA.

Color versions of one or more of the figures in this paper are available online at <http://ieeexplore.ieee.org>.

Digital Object Identifier 10.1109/TED.2018.2847230

**Index Terms**—2D material, interference effect, low-frequency (LF) vibration, Raman enhancement.

## I. INTRODUCTION

AFTER graphene was rediscovered, isolated, and characterized by Novoselov *et al.* [1], [2], 2D atomic crystals have risen as a new generation of materials with many impressive properties [3], [4]. Many novel 2D materials have been discovered and studied, such as hexagonal boron nitride (hBN) [5], germanane [6], transition metal dichalcogenides (TMDs) [7], [8], MXenes [9], and recently discovered magnetic 2D materials [10]. The variety of 2D materials allows us to build various types of heterojunction and homojunction to form a larger variety of material structures. For example, in the in-plane direction, “stitching” different 2D materials adjacent to each other builds an ultrathin heterojunction [11], [12]. In the out-of-plane direction, on the other hand, stacking 2D materials may introduce brand new physics, such as superconductivity at 1.7 K in  $1.1^\circ$  twisted bilayer graphene [13]. In these structures, interactions between atomic layers dramatically change the properties of the hybrid system [14], [15] and induce phenomena that are absent in individual layers. It has been reported that massive Dirac fermions and the Hofstadter butterfly emerge in graphene/hBN superlattices [16] and the interlayer excitons form in TMDs heterobilayers [17].

These 2D van der Waals heterostructures also show great promise in applications due to their excellent performance in optoelectronic devices superior to traditional materials systems [18]–[21].

Many explorations have been performed toward potentially new electronic properties of 2D van der Waals heterostructures [11]–[21]. In this context, it is significant to study their lattice vibrational properties that change the electronic performance of corresponding devices by affecting electron–phonon interactions. Thus, the new phonon modes in 2D heterostructures and their distinctive features have attracted much attention and have been characterized by Raman spectroscopy [15], [22]. It has been revealed that in the low frequency (LF) range ( $< \sim 100 \text{ cm}^{-1}$ ) of Raman spectra, there are shear modes and layer breathing modes created by interlayer interactions in layered graphene and TMDs [23]. However, to the best of our knowledge, the Raman modes of hBN–TMD heterostructure have not been reported yet. Besides, the substrates of the previous research are all dielectric materials, such as silicon or silicon oxide. The influence of metallic substrates on 2D van der Waals heterostructures has not been systematically discussed. Yet such a material structure is important for several reasons. First, hBN has been proven as an excellent dielectric layer to protect, stabilize, and isolate other 2D materials [24], which can assist 2D materials such as graphene and TMDs to achieve their best performance. Second, the metal substrate, due to its unique hot electrons and plasmonic features, can tune the properties of 2D materials differently from dielectric materials, such as quenching of photoluminescence (PL) of TMDs [25]. In addition, such a heterostructure TMD–hBN–metal forms a metal–oxide–semiconductor structure which is a basic building block of MOSFETs, and thus, the understanding of such a material system will provide important insights into device applications based on 2D heterostructures.

In this paper, we report the observation of interlayer phonon modes in atomically thin van der Waals heterostructures. We have measured both the low- and high-frequency Raman response of  $\text{WS}_2$ –hBN heterolayers on a gold film. Nineteen Raman modes are demonstrated, including a new LF mode at  $28.8 \text{ cm}^{-1}$ . The  $\text{WS}_2$  related Raman modes show a blue shift of about  $8 \text{ cm}^{-1}$  on our substrate compared to conventional substrates like silicon. Furthermore, we find that the Raman intensities of  $\text{WS}_2$  change remarkably with increasing the thickness of hBN. To better understand these experimental results, we perform a series of calculations, including first-principles calculations to explain the Raman modes, analytical calculation using transfer matrix, and finite-difference time-domain (FDTD) simulations to analyze the thickness dependence of Raman intensities. The integrated experimental/theoretical results reveal the influence of metallic substrate on 2D heterostructures and discover novel phonon modes between hBN and TMD layers. This paper provides an important guideline for the characterization of the 2D heterostructure and uncovers new vibrational properties of 2D materials, which is critical to the design and development of 2D electronic and optoelectronic devices.

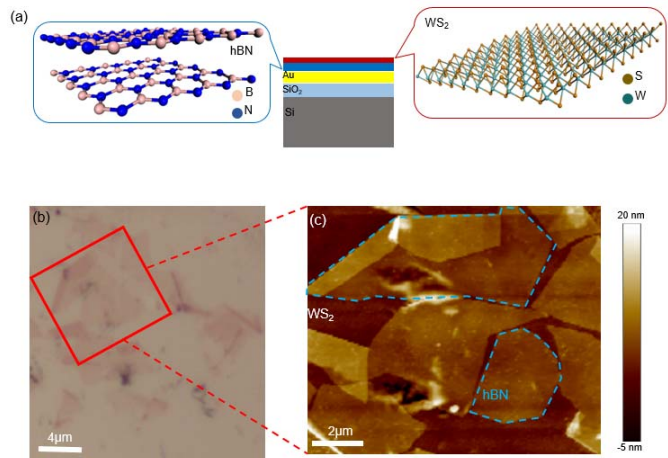


Fig. 1. (a) Schematic of the  $\text{WS}_2$ –hBN heterostructure: the atomic structures of hBN and  $\text{WS}_2$ , respectively. (b) Optical microscope image of the measured sample. (c) AFM photograph of  $\text{WS}_2$ –hBN sample, the areas circled around by blue dashed lines are hBN flakes and the whole area is covered by monolayer  $\text{WS}_2$ .

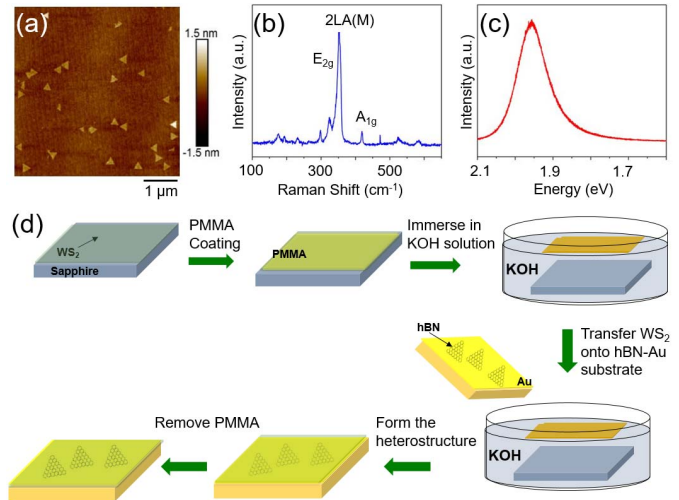
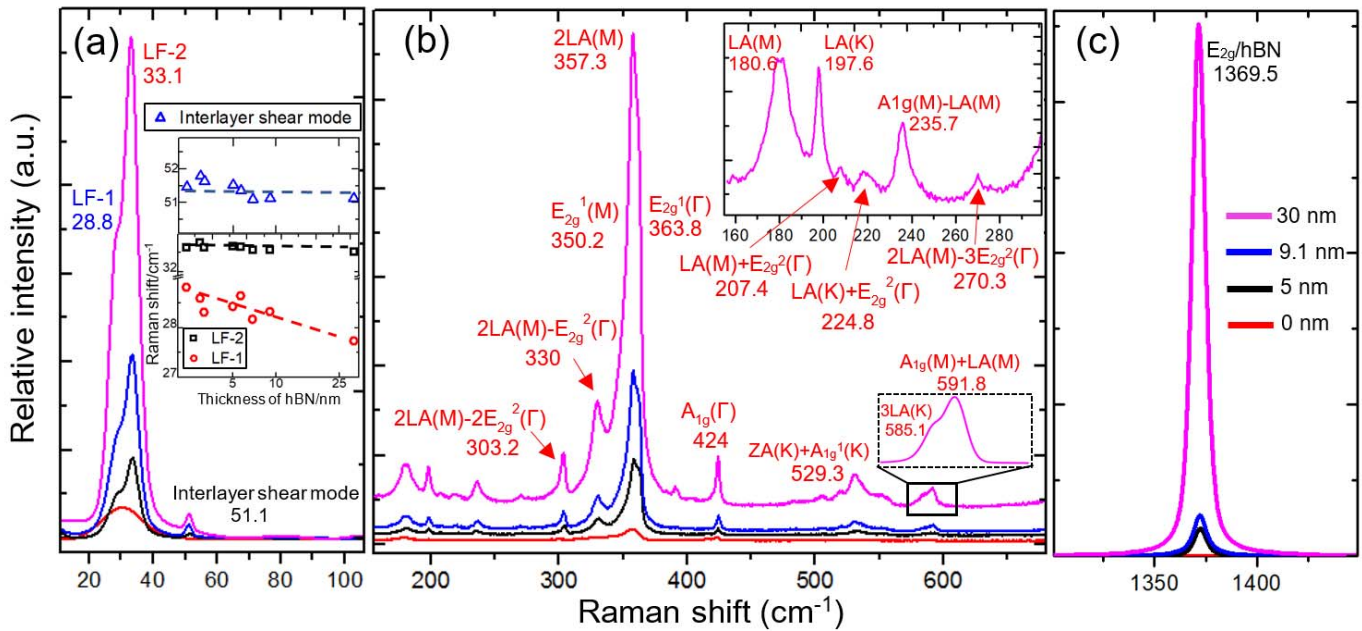


Fig. 2. (a) AFM image of CVD monolayer  $\text{WS}_2$  on the sapphire substrate. The small triangles are bilayer islands. (b) Raman and (c) PL spectra of as-grown monolayer  $\text{WS}_2$ . The Raman modes  $2\text{LA(M)}$ ,  $E_{2g}$  and  $A_{1g}$  of  $\text{WS}_2$  are labeled. (d) Flowchart of sample transfer process.

## II. EXPERIMENTAL MEASUREMENT

### A. Sample Preparation

The van der Waals heterostructure in this paper consists of few to multilayers of hBN and a monolayer of  $\text{WS}_2$  on 50-nm gold layer on the  $\text{SiO}_2/\text{Si}$  substrate, as shown in Fig. 1(a). The preparation process of the hBN– $\text{WS}_2$  heterostructure can be seen from Fig. 2. The hBN sheets are mechanically exfoliated from the bulk crystals onto the gold film which was deposited by electron beam evaporation on the silicon substrate covered by 300-nm-thick silicon dioxide. The monolayer  $\text{WS}_2$  is synthesized by gas source chemical vapor deposition (CVD) on 2-inch *c*-plane sapphire [(0001)  $\alpha\text{-Al}_2\text{O}_3$ ] substrate. Growth of monolayer  $\text{WS}_2$  was conducted employing a multistep growth process similar to that reported by Zhang *et al.* [27] for  $\text{WSe}_2$  growth, but with tungsten hexacarbonyl ( $\text{W}(\text{CO})_6$ ) and



**Fig. 3.** Lattice vibrations of  $\text{WS}_2$ -hBN heterostructure. (a) Raman spectra with different hBN thicknesses in LF ranging from 10 to  $105 \text{ cm}^{-1}$ . (b) and (c) Raman spectra with different hBN thicknesses at the frequency of  $155\text{--}680 \text{ cm}^{-1}$  and  $1300\text{--}1455 \text{ cm}^{-1}$ . In (c), curves with different colors correspond to different thicknesses of hBN. Nineteen Raman modes with mode assignments and Raman frequencies are marked in Raman spectrum. The Raman shifts (in units of  $\text{cm}^{-1}$ ) used here are results when hBN thickness is 30 nm. In (a)–(c), the red labeled modes originate from monolayer  $\text{WS}_2$ , the black labeled modes belong to hBN layers, and the blue labeled one is a special mode in  $\text{WS}_2$ -hBN heterostructure. Inset in (a): Raman shifts of the LF-1 mode, the LF-2 mode, and the interlayer shear mode with several hBN thicknesses.

hydrogen sulfide ( $\text{H}_2\text{S}$ ) as precursors diluted in hydrogen ( $\text{H}_2$ ) carrier gas with nucleation at  $850 \text{ }^\circ\text{C}$  and lateral growth at  $1000 \text{ }^\circ\text{C}$  [27] at a total reactor pressure of 50 torr. Partial pressures of  $\text{W}(\text{CO})_6$  and  $\text{H}_2\text{S}$  in the reactor chamber were  $7 \times 10^{-7}$  and 4.3 torr, respectively. The total deposition time [nucleation (30 s) + ripening (30 min) + lateral growth (30 min)] was 60.5 min. Samples were cooled to  $300 \text{ }^\circ\text{C}$  in the presence of  $\text{H}_2\text{S}$  to suppress possible decomposition of the  $\text{WS}_2$ . The high quality of the CVD  $\text{WS}_2$  is confirmed by characterization using atomic force microscopy (AFM) and Raman and PL spectroscopies, as shown in Fig. 2(a)–(c), respectively. The strong PL signal of monolayer  $\text{WS}_2$  with its characteristic emission energy at  $\sim 1.95 \text{ eV}$  demonstrates the good quality of our monolayer sample, which is a reliable guarantee for the follow-up experimental results [26]. We then transfer the CVD  $\text{WS}_2$  layer onto hBN-Au substrate, and the process is depicted in Fig. 2(d) [28]. To do this, we spin-coat polymethylmethacrylate (PMMA) on the  $\text{WS}_2$  flakes and peel them off from the sapphire substrate in heated potassium hydroxide (KOH) solution. The temperature of KOH solution is about  $85 \text{ }^\circ\text{C}$ . After rinsing the PMMA/ $\text{WS}_2$  layer in deionized water several times, we use the target substrate, which is the gold-coated silicon with hBN flakes on the surface mentioned earlier, to fish out the PMMA/ $\text{WS}_2$  layer floating on water. Due to the large number of hBN flakes exfoliated on gold film and the large area of  $\text{WS}_2$  film (centimeter scale), we are able to get many  $\text{WS}_2$ -hBN heterostructures on the gold substrate in one transfer. The obtained sample is soaked in the acetone solution to remove the PMMA layer. We further anneal the sample in  $250 \text{ }^\circ\text{C}$  for 3 h, in the  $\text{Ar}_2/\text{H}_2$  atmosphere with 100-sccm flow rate and a pressure of 500 mtorr. Through

this annealing process, residual stress is released and the possible residual chemicals in the interlayer space are removed, which finally gives rise to stronger coupling, and this will be discussed later in this paper. We use optical microscope to examine the sample and choose several spots of  $\text{WS}_2$ -hBN heterostructures through optical imaging contrast [Fig. 1(b)]. AFM is then used to characterize the sample and determine the thickness of hBN flakes [Fig. 1(c)]. The thicknesses of hBN flakes in chosen spots range from 0 to 30 nm.

### B. Spectra Measurement

The Raman and PL spectra of our samples are measured by a Raman spectrometer Horiba Evolution in ambient conditions. The Raman setup with 1800 lines/mm grating provides access to the spectral resolution of  $\sim 0.5 \text{ cm}^{-1}$ , and an ultra-LF filter enables the measurement of Raman shifts down to  $10 \text{ cm}^{-1}$ . The wavelength of excitation laser is  $532.5 \text{ nm}$ , which focuses on samples with a spot size of  $\sim 1 \text{ } \mu\text{m}$  and an incident power of  $\sim 1 \text{ mW}$ .

## III. RESULTS AND DISCUSSION

### A. Raman Spectra

The Raman spectra over a range of  $10\text{--}1450 \text{ cm}^{-1}$  at room temperature with different hBN thickness are displayed in Fig. 3. Nineteen Raman modes are presented in Fig. 3(a)–(c), including the first-order modes LA(M), LA(K) (longitudinal acoustic modes),  $E_{2g}^1(\Gamma)$ ,  $E_{2g}^1(\text{M})$ , and  $A_{1g}(\Gamma)$ , the second-order mode of  $2\text{LA}(\text{M})$ , LF modes of LF-1, LF-2, and the interlayer shear mode, and some combinational modes [26], [29].

For the high-frequency part ( $>100\text{ cm}^{-1}$ ), compared with our as-grown monolayer  $\text{WS}_2$  on sapphire and reported modes of monolayer  $\text{WS}_2$  and hBN on silicon [26], [29], Raman modes in the heterostructure show an obvious blue shift of about  $8\text{ cm}^{-1}$  for every  $\text{WS}_2$  mode. This suggests that the blue shift here is related to the substrate of our sample, which possibly changes the strength of dipolar interaction between the monolayer  $\text{WS}_2$  and the fixed charges in the substrate [30]. The influence of strain released after the transfer and annealing process may also contribute to the blue shift in the Raman modes of  $\text{WS}_2$ . In contrast, for the  $E_{2g}$  mode and the interlayer shear mode of hBN, the Raman shifts ( $1369.5$  and  $51.1\text{ cm}^{-1}$ ) do not change for different hBN thicknesses, which match well with [29]. Not just on the gold substrate, Galbiati *et al.* [31] have reported that the  $E_{2g}$  mode of hBN layers is also unchanged on copper. These phenomena reveal that the metallic substrate has little effect on Raman modes of the hBN layers. Taking account of the dielectric properties and wide bandgap of hBN layers, the fixed charges provided by the metallic substrate cause no changes. It is a convincing verification for our understanding of the role hBN–Au substrate played in the blue shift of Raman frequency for  $\text{WS}_2$ -related modes.

For the LF range of Raman spectra ( $<100\text{ cm}^{-1}$ ), modes at  $28.8$ ,  $33.1$ , and  $51.1\text{ cm}^{-1}$  are observed. The labeled LF-1 mode at  $28.8\text{ cm}^{-1}$  demonstrates resonance dependence on the hBN thickness and disappears when there is no hBN. The reason is that this mode originates from the interlayer shearing motion between monolayer  $\text{WS}_2$  and hBN layers, which is further confirmed by the redshift of this mode with thicker hBN [inset of Fig. 3(a) (red circles)]. The second mode at  $33.1\text{ cm}^{-1}$  (LF-2) is the intrinsic mode of monolayer  $\text{WS}_2$ , as the peak intensity and frequency remain with increasing the thickness of hBN, including the case without hBN, as seen from the inset of Fig. 3(a) (black squares). Referring to the previous research, Li *et al.* [32] and O'Brien *et al.* [33] reported the similar mode at LF in monolayer  $\text{WS}_2$ . The origin of this mode was explained by the resonant process due to the small spin–orbit splitting in the conduction band at K and K' points in  $\text{WS}_2$  [33]. The spin–orbit splitting for monolayer  $\text{WS}_2$  is about  $4\text{ meV}$  [34], which is in agreement with experimental data at  $33.1\text{ cm}^{-1}$ . The  $51.1\text{ cm}^{-1}$  mode is from interlayer shearing vibration in different hBN layers, which was discovered by Stenger *et al.* [29]. In [29], the measured Raman shift of this LF mode keeps unchanged at  $\sim 52\text{ cm}^{-1}$  after the layer number of hBN is above 10. This means that when the thickness of hBN is larger than  $3.2\text{ nm}$ , the Raman peak frequency is saturated, and this phenomenon can be clearly seen in Fig. 3(a) [inset (blue triangles)].

It is important to point out that the annealing process is significant for achieving a good interlayer coupling in the transferred 2D van der Waals heterostructures. Fig. 4 shows the comparison between the annealed sample and the same sample before annealing. For the LF-1 mode, the Raman spectra of the annealed sample has higher intensity and narrower linewidth: before annealing, the intensity is  $4760$  counts [purple line in Fig. 4(a)] for  $20\text{ s}$  accumulation time and the peak width is  $8.4\text{ cm}^{-1}$  when the hBN thickness is  $30\text{ nm}$ . However, after

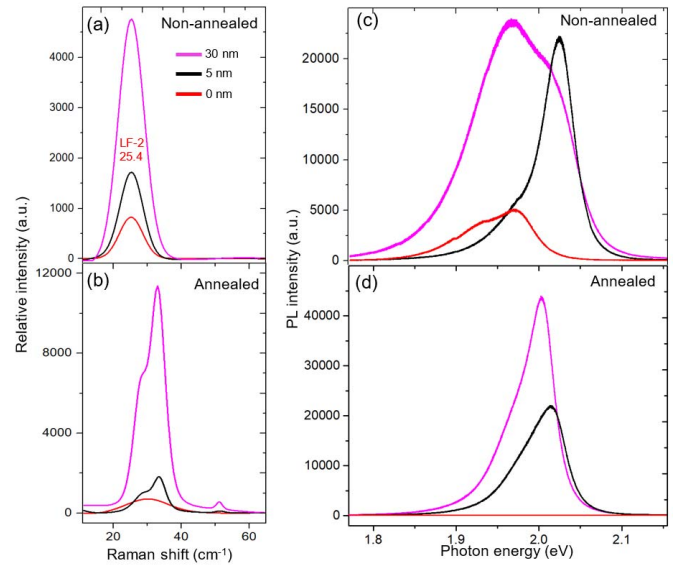
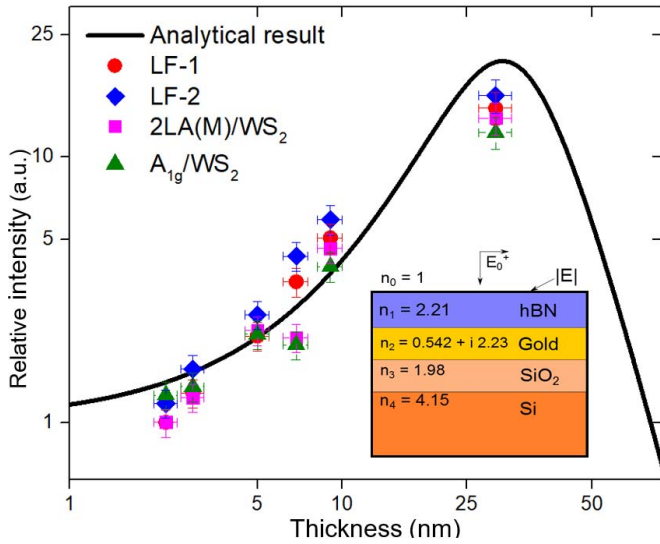


Fig. 4. Comparison of annealed and nonannealed samples. (a) and (b) Raman spectra of nonannealed and annealed samples at frequency ranging from  $10$  to  $65\text{ cm}^{-1}$ . (c) and (d) PL spectra of annealed and nonannealed sample. The purple, blue, and black lines indicate that the thickness of hBN in heterostructure is  $30$ ,  $5$ , and  $0\text{ nm}$  (no hBN), respectively.

annealing, the intensity enhances to  $11367$  counts [purple line in Fig. 4(b)] for the same accumulation time and the peak width decreases to  $4.2\text{ cm}^{-1}$ . Besides, we can see that compared with the annealed sample, the nonannealed sample only shows the LF-2 mode intrinsic to monolayer  $\text{WS}_2$  with redshift, and the LF-1 mode at around  $28.8\text{ cm}^{-1}$  is absent. The reason is that the absent LF-1 mode is relevant to the interaction between  $\text{WS}_2$  and hBN. After direct transfer, the coupling of the monolayer  $\text{WS}_2$  and hBN layers is not strong, and there are many impurities in the heterostructure which is not able to afford interlayer vibrations among the heterolayers. The annealing process can effectively remove impurities and enhance the coupling between  $\text{WS}_2$  and hBN in the heterostructure. Besides, the inferior condition of the interface increases extra energy dissipation for the LF-2 mode of  $\text{WS}_2$  which would result in the reduction of the vibration frequency, in other words, smaller Raman shift. Besides LF Raman modes, the PL spectra also dramatically changed after annealing. As seen from Fig. 4(c) and (d), the nonannealed sample shows parasitic PL peaks, and the PL shapes vary widely for different thicknesses, possibly due to the residual solution and residual strain in the heterostructure [35]. These experimental results verify that the annealing process plays an important role in sample preparations of the van der Waals atomic layer materials.

## B. Photoluminescence

Figs. 1(c) and 4(d) exhibit the representative PL spectra of as-grown monolayer  $\text{WS}_2$  on sapphire and constructed  $\text{WS}_2$ -hBN heterostructure on gold at room temperature. To better understand the origin of Raman modes and the interaction between monolayer  $\text{WS}_2$  and hBN layers, we have measured the Raman and PL spectra on several heterostructures with several hBN thicknesses. The measured PL comes from



**Fig. 5.** Intensity of Raman modes as a function of thickness of hBN. Four color spots represent the LF-1 mode, the LF-2 mode, the interlayer shear mode of hBN, and the  $A_{1g}$  mode of  $WS_2$ , respectively. The black line indicates the analytical result. The relative intensities of experimental and analytical results have been normalized. Inset: heterostructures for analytical calculations of the electric field strength on the surface of heterostructure  $|E|$  by using transfer matrix method.  $E_0^+$  is the incident electric field coming from vacuum  $n_0$ .

the excitons and trions at 2 and 1.98 eV, respectively, across a direct band gap of monolayer  $WS_2$  at the K and K' valleys of their band structures. For the  $WS_2$ -hBN heterostructure, we can find that PL spectra curves of different hBN thicknesses are similar to each other in spectral shape with emission energy peak at  $\sim 2.01$  eV. Due to the excitation laser energy of 2.33 eV which is much smaller than the bandgap of hBN, the obtained PL completely originates from the monolayer  $WS_2$  of the structure. We can also find that the PL intensity increases with increasing hBN thickness, which is probably caused by the influence of the interference effect as well. The obvious PL suppression measured in  $WS_2$  directly on Au indicates that the rate of charge transfer is directly affected by the distance between the monolayer  $WS_2$  and the gold film.

### C. Enhancement Effects

In Fig. 3(a)–(c), we can find that the intensity of the Raman response increases with increased thickness of hBN layers. As shown in Fig. 3(a), the LF modes LF-1 and LF-2 have an intensity increase of 6.8 and 6.2 times, respectively, with increasing thickness from 5 to 30 nm of hBN. For the high-frequency modes of  $WS_2$ , similar effects can be observed. For example, the  $A_{1g}$  mode of  $WS_2$  at  $424\text{ cm}^{-1}$  has an intensity increase of 5.6 times with increasing thickness from 5 to 30 nm of hBN. For the LF and high-frequency Raman modes of hBN at  $51.1\text{ cm}^{-1}$  [Fig. 3(a)] and  $1369.5\text{ cm}^{-1}$  [Fig. 3(c)], their intensities also increase, 5.7 and 19.5 times with increasing thickness from 5 to 30 nm of hBN.

In Fig. 5, we summarize the intensities of different Raman modes as a function of hBN thickness measured in the experiments. We also show the analytical calculation results by solid line for comparison, and the calculation method is described in detail in the later part of this paper. Fig. 5 demonstrates the

evolutions of relative Raman intensity with increasing thickness of hBN for the LF-1 mode (red circles), the LF-2 mode (blue diamonds), the 2LA mode of  $WS_2$  (purple squares), and the  $A_{1g}$  mode of  $WS_2$  (green triangles). These modes we choose represent different vibrational motions including intralayer (the first-order mode  $A_{1g}$ , the second-order mode 2LA(M), and the LF mode LF-2 in monolayer  $WS_2$ ) and interlayer (the interlayer shear mode LF-1 between monolayer  $WS_2$  and hBN layers). Considering that the intrinsic modes of hBN have stronger Raman response with more layers (the  $E_{2g}$  mode and the interlayer shear mode), we only focus on  $WS_2$  related modes to study the unique enhancement effect of  $WS_2$ -hBN heterostructure. We can find that larger Raman intensity is obtained for thicker hBN layers for hBN thickness smaller than 30 nm, and this monotonically increasing relationship applies to all different modes, whether it is at LF or not. Furthermore, the enhancement effect of Raman signal becomes stronger with more layers of hBN in the studied heterostructure. When the thickness of hBN increases from 2.3 to 30 nm, the LF-1 mode, the LF-2 mode, the interlayer shear mode of hBN, and the  $A_{1g}$  mode of  $WS_2$  have been enhanced 15, 16, 12, and 9 times, respectively. The remarkable enhancement of Raman intensity reveals the resonance effect of hBN layers on Raman response. The hBN layers that separate monolayer  $WS_2$  and gold film form an optical cavity to strengthen the incident and scattered light, thus enhancing Raman intensity in the heterostructure. Different from the previous research, a metallic interface is introduced into the 2D van der Waals structure. The metallic interface under the heterostructure contributes significantly to the enhancement of Raman signals.

### D. Analytical and Numerical Calculations

Here, we describe analytical calculations on the interference effect that is plotted by the solid curve in Fig. 5. The Raman intensity on the monolayer TMD depends on the strength of electric field on the surface of the heterostructure. The electric field on the surface of the heterostructure, as shown in Fig. 5, can be calculated by using the transfer matrix method [36]. Therefore, we can write the following equation:

$$\begin{bmatrix} E_0^+ \\ E_0^- \end{bmatrix} = [M_0][P_1][M_1][P_2][M_2][P_3][M_3] \begin{bmatrix} E_4^+ \\ 0 \end{bmatrix} \quad (1)$$

$$= \begin{bmatrix} a & b \\ c & d \end{bmatrix} \begin{bmatrix} E_4^+ \\ 0 \end{bmatrix} \quad (2)$$

where  $E_0^+$  and  $E_0^-$  are electric fields for the forward and the backward electromagnetic waves on the surface of the heterostructure, respectively, and  $E_4^+$  is the electric field transmitted to the silicon layer.  $E_0^+$  can also be considered as the incident electric field. The matrices  $[M_i]$  and  $[P_i]$  are  $2 \times 2$  matrices called the matching and propagation matrices, respectively, and given as

$$[M_i] = \frac{1}{2} \begin{bmatrix} 1 + n_{i+1}/n_i & 1 - n_{i+1}/n_i \\ 1 - n_{i+1}/n_i & 1 + n_{i+1}/n_i \end{bmatrix} \quad (3)$$

$$[P_i] = \begin{bmatrix} e^{-jk_i d_i} & e^{jk_i d_i} \\ e^{jk_i d_i} & e^{-jk_i d_i} \end{bmatrix} \quad (4)$$

where  $n_i$  and  $d_i$  are the refractive index and thickness of the  $i$ th medium and  $k_i = 2\pi n_i/\lambda$  is the wave vector of light inside

the  $i$ th medium. The refractive index of each medium is shown in the inset of Fig. 5. The thicknesses of gold and SiO<sub>2</sub> are adopted by  $d_2 = 50$  nm and  $d_3 = 300$  nm, respectively. From (1) and (2), we can obtain the strength of electric field on the surface of heterostructure as  $|E| = |E_0^+ + E_0^-|$ , where  $E_0^- = c/aE_0^+$ . In Fig. 5, we plot the enhancement of the electric field strength on the surface of heterostructure  $(|E/E_0^+|)^4$  as a function of thickness of hBN (black line) due to the electric field dependence of Raman intensity  $I \propto |E|^4$ . We can see from Fig. 5 that the experimental data are in good agreement with the analytical result, which confirms the enhancement effect in WS<sub>2</sub>-hBN heterostructure.

To better understand the mechanism of metallic interface in the enhancement effect of hBN layers, numerical simulations by FDTD have been carried out too. Considering the fact that the Raman intensity is actually detected optical signals, we use FDTD methods to simulate the heterostructure model. The simulation model is the same as Fig. 1(a). The permittivity of gold comes from the Johnson and Christy model [37], while the silicon substrate and covered oxide layer are calculated by the Palik model [38]. The optical parameters of hBN and WS<sub>2</sub> are derived from experimental data from [39]. The 0.6-nm-thick monolayer WS<sub>2</sub> on various thicknesses of hBN layer shapes the WS<sub>2</sub>-hBN heterostructure. The thickness of gold film and SiO<sub>2</sub> on the semi-infinite thickness silicon substrate is 50 and 300 nm. The excitation light is linear polarized and the wavelength is 532.5 nm consistent with experimental conditions. It is worth noting that, because it is hard to set strictly monochromatic light in FDTD simulations, we use a narrowband light from 510 to 554 nm in wavelength here, with intensity peak at 532.5 nm. The Raman spectroscopy we used in measurement is reflection type, so we calculate reflection spectra to simulate the scattering and hBN cavity interference effect. To eliminate the environmental background, we calculate the reflection contrast of the WS<sub>2</sub>-hBN heterostructure with different hBN thicknesses to study the enhancement effect. The reflection contrast is given as

$$\Delta R = (R_{\text{substrate}} - R_{\text{sample}})/R_{\text{substrate}} \quad (5)$$

where substrate means the 50-nm-thick gold film on SiO<sub>2</sub>/Si. The results of FDTD simulations are shown in Fig. 6. The reflection contrast increases with thicker hBN, consistent with experimental results and analytical calculations shown in Fig. 5. There are three peaks in Fig. 6 labeled A, B, and C. The peak A at 2.01 eV and B at 2.4 eV are WS<sub>2</sub> excitonic absorption peaks arising from direct-gap transitions at the K point. The energy difference between the peak A and B indicates the strength of spin-orbit interaction which is approximately 400 meV for WS<sub>2</sub> in reasonable agreement with the calculations [40]. The additional peak C which is calculated around 2.85 eV originates from optical transitions between the density of states peaks in the valence and conduction bands in WS<sub>2</sub> [41]. Similar to experimental results of monolayer WS<sub>2</sub> by Zhao *et al.* [42], the magnitudes of reflection contrast for peaks B and C in Fig. 6 (labeled as 0 nm) are closer to that of the peak A. However, the situation changes when the hBN layer is added. The peak in higher energy or smaller

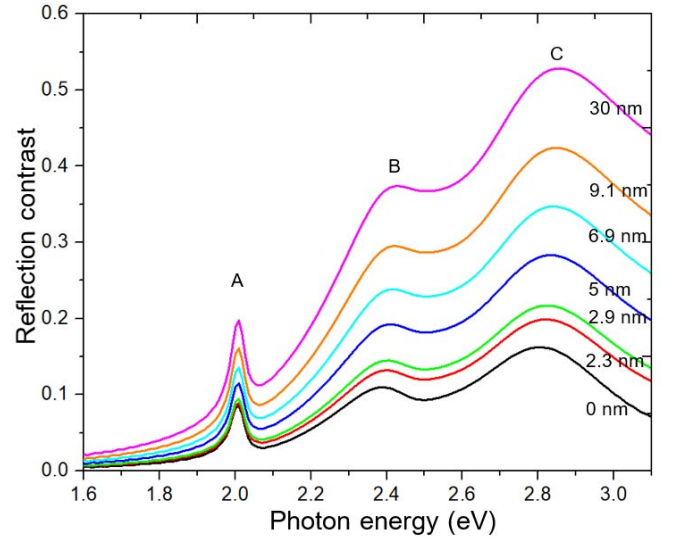


Fig. 6. FDTD simulation results of reflection contrast of the WS<sub>2</sub>-hBN heterostructure with different hBN thicknesses on a gold film. The different color lines indicate different thicknesses of hBN layer ranging from 0 (no hBN) to 30 nm. There are three peaks at 2.01, 2.4, and 2.85 eV labeled A, B, and C, respectively.

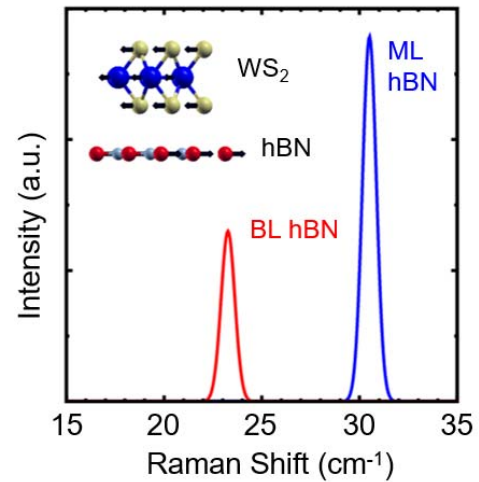


Fig. 7. Raman spectra of the interlayer shearing mode from *ab initio* density-functional calculation for monolayer WS<sub>2</sub> on monolayer hBN (blue peak) and on bilayer hBN (red peak).

wavelength has a faster increase in reflection contrast with the increase of hBN thickness. This effect is attributed to the wavelength dependent resonance of hBN-Au cavity, which also contributes to the enhancement of Raman intensity of the monolayer TMD on the top of this cavity.

### E. First-Principles Calculations

To confirm the LF shearing mode in the WS<sub>2</sub>-hBN heterostructure, we performed *ab initio* density-functional calculations on the lattice dynamics of the hybrid system. Considering that the lattice incommensurability existing between WS<sub>2</sub> ( $a_0 = 5.91$  Bohr) and hBN ( $a_0 = 4.70$  Bohr) has no pronounced effect on the interlayer shearing mode, but increases substantially the computational cost for studying lattice dynamics, we used a small unit cell with hBN at

equilibrium but WS<sub>2</sub> at a compressive strain. The nonresonant Raman spectra were calculated based on the density-functional perturbation theory [43] and Placzek approximation as introduced by Lazzeri and Mauri [44]. Fig. 7 shows the Raman spectra of the shearing mode and its change with a number of hBN layers. Raman mode is red-shifted with increasing the number of hBN layers, which agrees with the experimental results shown in Fig. 3. Note that the frequency shift is slightly bigger ( $\Delta\omega \sim 8 \text{ cm}^{-1}$ ) than the experimental data ( $\Delta\omega \sim 1 \text{ cm}^{-1}$ ), which may come from the lattice stress and the smaller number of hBN layers in calculation than in the experiment.

#### IV. CONCLUSION

In this paper, we systemically studied the Raman modes in van der Waals heterostructures formed by layered hBN and monolayer WS<sub>2</sub> on the gold substrate, combining experiments, numerical and analytical modeling, and first-principles calculations. The Raman spectroscopy has been employed to characterize our heterostructure. We observed 19 Raman modes including some new Raman modes which are first reported. Through the analysis of experimental data of the Raman response with different hBN thicknesses, we find Raman intensity increases with increasing thickness of hBN layers. A series of simulations and theoretical calculations have been performed to explain the new vibrational modes and reveal the physical mechanism of the remarkable enhancement effect in WS<sub>2</sub>-hBN heterostructure. We propose a new vibration mode and the analytical calculations are in good agreement with experimental results. The metallic surface and hBN layers form an optical cavity enhance Raman signals. The relation between Raman intensity and thickness of hBN layers provides a new way to enhance Raman signals of TMD monolayers. Our research clearly demonstrates the influence of substrates on the Raman modes of TMD monolayers which also opens the possibility of characterizing nanoscale van der Waals crystal structures with Raman spectroscopy. Through stacking different 2D crystals on metallic substrates, specific 2D materials can be obtained with desirable properties that are absent in natural crystals.

#### REFERENCES

- [1] K. S. Novoselov *et al.*, "Electric field effect in atomically thin carbon films," *Science*, vol. 306, no. 5696, pp. 666–669, 2004, doi: [10.1126/science.1102896](https://doi.org/10.1126/science.1102896).
- [2] K. S. Novoselov *et al.*, "Two-dimensional gas of massless Dirac fermions in graphene," *Nature*, vol. 438, no. 7065, pp. 197–200, Nov. 2005, doi: [10.1038/nature04233](https://doi.org/10.1038/nature04233).
- [3] K. S. Novoselov, V. I. Fal'ko, L. Colombo, P. R. Gellert, M. G. Schwab, and K. Kim, "A roadmap for graphene," *Nature*, vol. 490, p. 192, Oct. 2012, doi: [10.1038/nature11458](https://doi.org/10.1038/nature11458).
- [4] S. Z. Butler *et al.*, "Progress, challenges, and opportunities in two-dimensional materials beyond graphene," *ACS Nano*, vol. 7, no. 4, pp. 2898–2926, 2013, doi: [10.1021/nn400280c](https://doi.org/10.1021/nn400280c).
- [5] M. Kawaguchi, S. Kuroda, and Y. Muramatsu, "Electronic structure and intercalation chemistry of graphite-like layered material with a composition of BC<sub>6</sub>N," *J. Phys. Chem. Solids*, vol. 69, nos. 5–6, pp. 1171–1178, 2008, doi: [10.1016/j.jpcs.2007.10.076](https://doi.org/10.1016/j.jpcs.2007.10.076).
- [6] E. Bianco, S. Butler, S. Jiang, O. D. Restrepo, W. Windl, and J. E. Goldberger, "Stability and exfoliation of germanane: A germanium graphene analogue," *ACS Nano*, vol. 7, no. 5, pp. 4414–4421, May 2013, doi: [10.1021/nn4009406](https://doi.org/10.1021/nn4009406).
- [7] K. F. Mak, C. Lee, J. Hone, J. Shan, and T. F. Heinz, "Atomically thin MoS<sub>2</sub>: A new direct-gap semiconductor," *Phys. Rev. Lett.*, vol. 105, no. 13, p. 136805, Sep. 2010, doi: [10.1103/PhysRevLett.105.136805](https://doi.org/10.1103/PhysRevLett.105.136805).
- [8] L. Zhou *et al.*, "Sensitive phonon-based probe for structure identification of 1T' MoTe<sub>2</sub>," *J. Amer. Chem. Soc.*, vol. 139, no. 25, pp. 8396–8399, May 2017, doi: [10.1021/jacs.7b03445](https://doi.org/10.1021/jacs.7b03445).
- [9] M. Naguib *et al.*, "Two-dimensional nanocrystals produced by exfoliation of Ti<sub>3</sub>AlC<sub>2</sub>," *Adv. Mater.*, vol. 23, no. 37, pp. 4248–4253, Aug. 2011, doi: [10.1002/adma.201102306](https://doi.org/10.1002/adma.201102306).
- [10] K. L. Seyler *et al.*, "Ligand-field helical luminescence in a 2D ferromagnetic insulator," *Nature Phys.*, vol. 14, no. 3, pp. 277–281, Mar. 2018, doi: [10.1038/s41567-017-0006-7](https://doi.org/10.1038/s41567-017-0006-7).
- [11] X. Ling *et al.*, "Parallel stitching of 2D materials," *Adv. Mater.*, vol. 28, no. 12, pp. 2322–2329, Jan. 2016, doi: [10.1002/adma.201505070](https://doi.org/10.1002/adma.201505070).
- [12] K. S. Novoselov, A. Mishchenko, A. Carvalho, and A. C. Neto, "2D materials and van der Waals heterostructures," *Science*, vol. 353, no. 6298, p. aac9439, Jul. 2016, doi: [10.1126/science.aac9439](https://doi.org/10.1126/science.aac9439).
- [13] Y. Cao *et al.*, "Unconventional superconductivity in magic-angle graphene superlattices," *Nature*, vol. 556, no. 7699, pp. 43–50, Apr. 2018, doi: [10.1038/nature26160](https://doi.org/10.1038/nature26160).
- [14] S. Huang *et al.*, "Probing the interlayer coupling of twisted bilayer MoS<sub>2</sub> using photoluminescence spectroscopy," *Nano Lett.*, vol. 14, no. 10, pp. 5500–5508, Aug. 2014, doi: [10.1021/nl5014597](https://doi.org/10.1021/nl5014597).
- [15] S. Huang *et al.*, "Low-frequency interlayer Raman modes to probe interface of twisted bilayer MoS<sub>2</sub>," *Nano Lett.*, vol. 16, no. 2, pp. 1435–1444, Jan. 2016, doi: [10.1021/acs.nanolett.5b05015](https://doi.org/10.1021/acs.nanolett.5b05015).
- [16] L. A. Ponomarenko *et al.*, "Cloning of Dirac fermions in graphene superlattices," *Nature*, vol. 497, pp. 594–597, May 2013, doi: [10.1038/nature12187](https://doi.org/10.1038/nature12187).
- [17] P. Rivera *et al.*, "Observation of long-lived interlayer excitons in monolayer MoSe<sub>2</sub>-WSe<sub>2</sub> heterostructures," *Nature Commun.*, vol. 6, Feb. 2015, Art. no. 6242, doi: [10.1038/ncomms7242](https://doi.org/10.1038/ncomms7242).
- [18] L. Britnell *et al.*, "Strong light-matter interactions in heterostructures of atomically thin films," *Science*, vol. 340, no. 6138, pp. 1311–1314, Jun. 2013, doi: [10.1126/science.1235547](https://doi.org/10.1126/science.1235547).
- [19] L. Britnell *et al.*, "Field-effect tunneling transistor based on vertical graphene heterostructures," *Science*, vol. 335, no. 6071, pp. 947–950, Feb. 2012, doi: [10.1126/science.1218461](https://doi.org/10.1126/science.1218461).
- [20] C.-H. Liu, Y.-C. Chang, T. B. Norris, and Z. Zhong, "Graphene photodetectors with ultra-broadband and high responsivity at room temperature," *Nature Nanotechnol.*, vol. 9, pp. 273–278, Mar. 2014, doi: [10.1038/nnano.2014.31](https://doi.org/10.1038/nnano.2014.31).
- [21] W. J. Yu *et al.*, "Highly efficient gate-tunable photocurrent generation in vertical heterostructures of layered materials," *Nature Nanotechnol.*, vol. 8, pp. 952–958, Oct. 2013, doi: [10.1038/nnano.2013.219](https://doi.org/10.1038/nnano.2013.219).
- [22] A. C. Ferrari, "Raman spectroscopy of graphene and graphite: Disorder, electron-phonon coupling, doping and nonadiabatic effects," *Solid State Commun.*, vol. 143, nos. 1–2, pp. 47–57, Apr. 2007, doi: [10.1016/j.ssc.2007.03.052](https://doi.org/10.1016/j.ssc.2007.03.052).
- [23] C. H. Lui *et al.*, "Observation of interlayer phonon modes in van der Waals heterostructures," *Phys. Rev. B, Condens. Matter*, vol. 91, no. 16, p. 165403, Apr. 2015, doi: [10.1103/PhysRevB.91.165403](https://doi.org/10.1103/PhysRevB.91.165403).
- [24] K. Zhang, Y. Feng, F. Wang, Z. Yang, and J. Wang, "Two dimensional hexagonal boron nitride (2D-hBN): Synthesis, properties and applications," *J. Mater. Chem. C*, vol. 5, no. 46, pp. 11992–12022, Nov. 2017, doi: [10.1039/C7TC04300G](https://doi.org/10.1039/C7TC04300G).
- [25] U. Bhanu, M. R. Islam, L. Tetard, and S. I. Khondaker, "Photoluminescence quenching in gold-MoS<sub>2</sub> hybrid nanoflakes," *Sci. Rep.*, vol. 4, Jul. 2014, Art. no. 5575, doi: [10.1038/srep05575](https://doi.org/10.1038/srep05575).
- [26] C. Cong *et al.*, "Synthesis and optical properties of large-area single-crystalline 2D semiconductor WS<sub>2</sub> monolayer from chemical vapor deposition," *Adv. Opt. Mater.*, vol. 2, no. 2, pp. 131–136, Dec. 2014, doi: [10.1002/adom.201300428](https://doi.org/10.1002/adom.201300428).
- [27] X. Zhang *et al.*, "Diffusion-controlled epitaxy of large area coalesced WSe<sub>2</sub> monolayers on sapphire," *Nano Lett.*, vol. 18, no. 2, pp. 1049–1056, Feb. 2018, doi: [10.1021/acs.nanolett.7b04521](https://doi.org/10.1021/acs.nanolett.7b04521).
- [28] F. Zhang, C. Erb, L. Runkle, X. Zhang, and N. Alem, "Etchant-free transfer of 2D nanostructures," *Nanotechnology*, vol. 29, no. 2, p. 025602, Dec. 2018, doi: [10.1088/1361-6528/aa9c21](https://doi.org/10.1088/1361-6528/aa9c21).
- [29] I. Stenger *et al.*, "Low frequency Raman spectroscopy of few-atomic-layer thick hBN crystals," *2D Mater.*, vol. 4, no. 3, p. 031003, Jun. 2017, doi: [10.1088/2053-1583/aa77d4](https://doi.org/10.1088/2053-1583/aa77d4).

- [30] M. Buscema, G. A. Steele, H. S. J. van der Zant, and A. Castellanos-Gomez, "The effect of the substrate on the Raman and photoluminescence emission of single-layer MoS<sub>2</sub>," *Nano Res.*, vol. 7, no. 4, pp. 561–571, Apr. 2014, doi: [10.1007/s12274-014-0424-0](https://doi.org/10.1007/s12274-014-0424-0).
- [31] M. Galbati, A. C. Stoot, D. M. A. Mackenzie, P. Bøggild, and L. Camilli, "Real-time oxide evolution of copper protected by graphene and boron nitride barriers," *Sci. Rep.*, vol. 7, Jan. 2017, Art. no. 39770, doi: [10.1038/srep39770](https://doi.org/10.1038/srep39770).
- [32] W.-F. Li, C. Fang, and M. A. van Huis, "Strong spin-orbit splitting and magnetism of point defect states in monolayer WS<sub>2</sub>," *Phys. Rev. B, Condens. Matter*, vol. 94, no. 19, p. 195425, Nov. 2016, doi: [10.1103/PhysRevB.94.195425](https://doi.org/10.1103/PhysRevB.94.195425).
- [33] M. O'Brien, N. McEvoy, D. Hanlon, T. Hallam, J. N. Coleman, and G. S. Duesberg, "Mapping of low-frequency Raman modes in CVD-grown transition metal dichalcogenides: Layer number, stacking orientation and resonant effects," *Sci. Rep.*, vol. 6, Jan. 2016, Art. no. 19476, doi: [10.1038/srep19476](https://doi.org/10.1038/srep19476).
- [34] S. Guo, Y. Wang, C. Wang, Z. Tang, and J. Zhang, "Large spin-orbit splitting in the conduction band of halogen (F, Cl, Br, and I) doped monolayer WS<sub>2</sub> with spin-orbit coupling," *Phys. Rev. B, Condens. Matter*, vol. 96, no. 24, p. 245305, Dec. 2017, doi: [10.1103/PhysRevB.96.245305](https://doi.org/10.1103/PhysRevB.96.245305).
- [35] K. M. McCreary *et al.*, "The effect of preparation conditions on Raman and photoluminescence of monolayer WS<sub>2</sub>," *Sci. Rep.*, vol. 6, Oct. 2016, Art. no. 35154, doi: [10.1038/srep35154](https://doi.org/10.1038/srep35154).
- [36] H. Liu, M. S. Ukhary, and R. Saito, "Hidden symmetries in N-layer dielectric stacks," *J. Phys., Condensed Matter*, vol. 29, no. 45, p. 455303, 2017, doi: [10.1088/1361-648X/aa865c](https://doi.org/10.1088/1361-648X/aa865c).
- [37] R. T. Beach and R. W. Christy, "Electron-electron scattering in the intraband optical conductivity of Cu, Ag, and Au," *Phys. Rev. B, Condens. Matter*, vol. 16, no. 12, p. 5277, Dec. 1977, doi: [10.1103/PhysRevB.16.5277](https://doi.org/10.1103/PhysRevB.16.5277).
- [38] E. D. Palik, *Handbook of Optical Constants of Solids*, 1st ed. San Diego, CA, USA: Academic, 1998, pp. 749–763.
- [39] Y. V. Morozov and M. Kuno, "Optical constants and dynamic conductivities of single layer MoS<sub>2</sub>, MoSe<sub>2</sub>, and WSe<sub>2</sub>," *Appl. Phys. Lett.*, vol. 107, no. 8, p. 083103, Aug. 2015, doi: [10.1063/1.4929700](https://doi.org/10.1063/1.4929700).
- [40] A. Ramasubramaniam, "Large excitonic effects in monolayers of molybdenum and tungsten dichalcogenides," *Phys. Rev. B, Condens. Matter*, vol. 86, no. 11, p. 115409, Sep. 2012, doi: [10.1103/PhysRevB.86.115409](https://doi.org/10.1103/PhysRevB.86.115409).
- [41] L. F. Mattheiss, "Band structures of transition-metal-dichalcogenide layer compounds," *Phys. Rev. B, Condens. Matter*, vol. 8, no. 8, p. 3719, Oct. 1973, doi: [10.1103/PhysRevB.8.3719](https://doi.org/10.1103/PhysRevB.8.3719).
- [42] W. Zhao *et al.*, "Evolution of electronic structure in atomically thin sheets of WS<sub>2</sub> and WSe<sub>2</sub>," *ACS Nano*, vol. 7, no. 1, pp. 791–797, Dec. 2012, doi: [10.1021/nn305275h](https://doi.org/10.1021/nn305275h).
- [43] S. Baroni, S. de Gironcoli, A. Dal Corso, and P. Giannozzi, "Phonons and related crystal properties from density-functional perturbation theory," *Rev. Mod. Phys.*, vol. 73, no. 2, pp. 515–562, Jul. 2001, doi: [10.1103/RevModPhys.73.515](https://doi.org/10.1103/RevModPhys.73.515).
- [44] M. Lazzeri and F. Mauri, "First-principles calculation of vibrational Raman spectra in large systems: Signature of small rings in crystalline SiO<sub>2</sub>," *Phys. Rev. Lett.*, vol. 90, no. 3, p. 036401, Jan. 2003, doi: [10.1103/PhysRevLett.90.036401](https://doi.org/10.1103/PhysRevLett.90.036401).



**Li Ding** received the bachelor's and Ph.D. degrees in physics from University of Science and Technology of China, Hefei, China, in 2011 and 2016, respectively.

He is currently a Post-Doctoral Scholar with The Pennsylvania State University, State College, PA, USA, under the supervision of Prof. S. Huang.

**Muhammad Shoufie Ukhary**, photograph and biography not available at the time of publication.



**Mikhail Chubarov** received the M.Sc. degree from the University of Latvia, Riga, Latvia, in 2010, and the Ph.D. degree in thin film physics from Linköping University, Linköping, Sweden, in 2015. His Ph.D. thesis was on growth and characterization of sp<sup>2</sup>-hybridized BN.

Since 2017, he has been holding a post-doctoral position at The Pennsylvania State University, State College, PA, USA.

**Tanushree H. Choudhury**, photograph and biography not available at the time of publication.

**Fu Zhang**, photograph and biography not available at the time of publication.



**Rui Yang** (S'13–M'18) received the bachelor's degree from Tianjin University, Tianjin, China, in 2011, and the Ph.D. degree in electrical engineering from Case Western Reserve University, Cleveland, OH, USA, in 2016.

He is currently a Tenure-Track Assistant Professor at the University of Michigan-Shanghai Jiao Tong University Joint Institute, Shanghai Jiao Tong University, Shanghai, China.

**Ao Zhang**, photograph and biography not available at the time of publication.



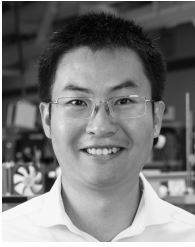
**Jonathan A. Fan** received the B.S.E. degree in electrical engineering from Princeton University, Princeton, NJ, USA, in 2004, and the M.S. and Ph.D. degrees in applied physics from Harvard University, Cambridge, MA, USA, in 2006 and 2010, respectively.

He is currently an Assistant Professor at Stanford University, Stanford, CA, USA, and is researching new materials and design concepts for electromagnetic devices.

**Mauricio Terrones**, photograph and biography not available at the time of publication.

**Joan M. Redwing** is a Faculty Member of materials science and engineering at The Pennsylvania State University, University Park, PA, USA. She serves as the Director of the 2-D Crystal Consortium–Materials Innovation Platform. She is an author of over 270 publications and holds eight U.S. patents. Her research interests include epitaxial growth of semiconductor thin films and nanomaterials by chemical vapor deposition.

**Teng Yang**, photograph and biography not available at the time of publication.



**Mingda Li** is currently an Assistant Professor of nuclear science and engineering at the Massachusetts Institute of Technology, Cambridge, MA, USA. His research group, the Energy Nano Group, aims to engineer materials quantum orders and functional properties through defect engineering, using combined spectroscopic and theoretical efforts toward low-energy dissipation energy applications.



**Shengxi Huang** received the bachelor's degree from Tsinghua University, Beijing, China, in 2011, and the Ph.D. degree from the Massachusetts Institute of Technology, Cambridge, MA, USA, in 2017 under the supervision of Prof. M. Dresselhaus.

She is currently an Assistant Professor with the Department of Electrical Engineering, The Pennsylvania State University, State College, PA, USA. Her current research interests include 2D materials, optical spectroscopy, and optoelectronic and sensing devices.



**Riichiro Saito** received the Ph.D. degree from The University of Tokyo, Tokyo, Japan, in 1985.

In 1990, he became an Associate Professor at the University of Electro-Communications, Tokyo. In 2003, he became a Professor of physics, Tohoku University, Sendai, Japan. In 1991 and 1992, he was a Visiting Scientist at the Massachusetts Institute of Technology, Cambridge, MA, USA, where he published pioneered papers of carbon nanotubes with Prof. G. Dresselhaus and Prof. M. S. Dresselhaus.